Research Article | Vol. 26, No. 23 | 12 Nov 2018 | OPTICS EXPRESS 29983
Optics EXPRESS

High sensitivity active flat optics optical phased array receiver with a two-dimensional aperture

REZA FATEMI,* BEHROOZ ABIRI, AROUTIN KHACHATURIAN, AND ALI HAJIMIRI

California Institute of Technology, 1200 E. California Blvd, Pasadena, CA 91125, USA
*sfatemi@caltech.edu

Abstract: Optical phased arrays (OPAs) on integrated photonic platforms provide a low-cost chip-scale solution for many applications. Despite the numerous demonstrations of OPA transmitters, the realization of a functional OPA receiver presents a challenge due to the low received signal level in the presence of noise and interference that necessitates high sensitivity of the receiver. In this paper, an integrated receiver system is presented that is capable of on-chip adaptive manipulation and processing of the captured waveform. The receiver includes an optoelectronic mixer that down-converts optical signals to radio frequencies while maintaining their phase and amplitude information. The optoelectronic mixer also provides conversion gain that enhances the system sensitivity and its robustness to noise and interference. Using this system, the first OPA receiver with a two-dimensional aperture of 8-by-8 receiving elements is demonstrated which can selectively receive light from 64 different angles. The OPA receiver can form reception beams with a beamwidth of 0.75° over an 8° grating-lobe-free field of view.

1. Introduction

Precise manipulation and engineering of optical wavefronts is an essential function of many optical systems to achieve desirable performance [1–4]. Conventionally, this task is performed by utilizing various discrete optical components such as lenses. However, an integrated system with active waveform engineering capability on a thin substrate reduces the size of many conventional optical systems which results in reduced cost, scalability, and better manufacturability [5–8]. Moreover, an active flat optics solution will further open the door for many applications and functionalities that were not practical previously [9–13].

Recently, OPA transmitters (TX) capable of electrical adaptive beamforming, forming a beam of light and steering it electronically, have attracted a great deal of interest [14–31]. An OPA transmitter consists of an array of radiating elements and can be used to engineer a desired optical wavefront. Such an optical transmitter has applications in systems such as LiDAR [28–32], point-to-point communication [26, 27, 33], lens-less projection [19], and holographic displays [34]. Large-scale OPA transmitters with more than a thousand radiating elements have been demonstrated with narrow beamwidth and high resolution [14–18]. Non-uniform element placement has enabled large steering range OPAs [17, 18] with the capability of steering the optical beam along both axial directions with over 65,000 resolvable spots. Moreover, an OPA transmitter in the visible range has also been demonstrated [15].

An OPA receiver (RX) is the counterpart to the OPA transmitter. It can form and steer a reception beam electronically and collect light selectively from any desired direction. It also suppresses undesirable light impinging on it from other directions, multipath reflections, or even active jammers. This spatially selective reception is highly valuable in many applications, such as LiDAR and point-to-point communication systems. The OPA receiver in a LiDAR system can be used to collect light from the spot that is being illuminated by the transmitter and reject all the unwanted illuminated points and multipath reflections, to enhance sensitivity that can directly translate to range and accuracy. An OPA receiver can also be beneficial in point-to-point

#338803 https://doi.org/10.1364/OE.26.029983
Journal © 2018 Received 16 Jul 2018; revised 25 Sep 2018; accepted 6 Oct 2018; published 31 Oct 2018

Optics EXPRESS

communication systems with multiple free-space optical communication systems to minimize the interference between channels and increase the fidelity of the communication system utilizing its selective directivity.

Moreover, an active flat optics OPA receiver also enables other applications that may not be feasible or practical with conventional optics, such as emulating a lens functionality on a flat active substrate (e.g., on a silicon chip) with negligible depth to perform lens-less imaging. This eliminates the need for lenses that are usually bulky and require sizable physical depth to form an image on the focal plane. The synthetic aperture formed by an active flat optics OPA receiver integrates the functionality of the lens on a very thin flat active area [35, 36].

Previously, an OPA transmitter was suggested to operate as a phased array receiver based on the reciprocity of electromagnetic wave propagation [37]. However, it does not provide the sensitivity necessary for a practical OPA receiver due to the fundamentally different design trade-offs for a transmitter and a receiver. Since signal levels at the receiver input are typically very weak, the performance of such a direct power detection receiver architecture suffers from out-of-band signals, stray light, noise, and other sources of interference.

In this work, an integrated photonics receiver architecture is developed that captures samples of the incident light on its aperture and can arbitrarily manipulate the optical wavefront on-chip. To detect weak received signals and achieve a high sensitivity, an integrated optoelectronic mixer is designed and used in the signal path to provide conversion gain and adjustable phase shift. The phase shift is tuned without introducing additional loss in the signal path by controlling the phase of a local optical reference. This approach enables detection of weak received signals in the presence of noise, interference, and stray light. The optoelectronic mixer converts the optical frequency of the captured samples to a lower RF frequency, which can be processed by electronic components while preserving phase and amplitude information. To demonstrate the capability of this system, the first high-sensitivity active flat optics OPA receiver with a two-dimensional aperture is implemented with an 8-by-8 array aperture [36]. Such a 2D active flat optics OPA receiver can perform functions such as directive reception and rejection of the incident wave impinging from a specific bearing as well as receive light from a single focused point in front of the aperture. Moreover, since the on-chip processing is electronically controllable, the system can perform the functionality of an adaptive lens, in which the shape of the lens can be changed to the desired shape. The performance of the OPA is characterized by forming directive reception beams at different elevations and azimuth angles. Moreover, it is configured to perform as an ultra-thin optical imaging system without the need for a bulky lens that scans its field of view (FOV) and images physical objects.

2. Theory of operation and system design

In this section, the theory of the receiver operation and the design of the 8-by-8 OPA receiver will be discussed. Figure 1(a) shows the general setting of the receiver system, where the impinging wavefront is coupled to the receiving elements arranged in a 2D array. Based on sampling theory, the properties of the incident electromagnetic wavefront can be reconstructed using samples of the measured waveform at a finite number of points, where the accuracy of the reconstruction is determined by the element spacing, the number of spatial samples, as well as the signal-to-noise ratio.

2.1. Receiver aperture

The receiver aperture consists of a set of receiving elements (i.e., nano-photonic antennas) placed on a planar surface. Each receiving element captures the optical electromagnetic wave incident on it and couples it to a waveguide on the chip (Fig. 2(a) shows the designed receiving element and the waveguide that it couples the captured light into it). In a receiver with a uniform aperture

Optics EXPRESS

grid, elements are located at

$$(x_n, y_m) = (nd, md), \quad 0 \le n < N, \qquad 0 \le m < M, \tag{1}$$

where n, m, N, and M are integer numbers and d is the element spacing (In general, the spacing between elements can be non-uniform, forming an aperiodic or a sparse array. Such apertures has been used for OPA transmitters [17, 18] to scale the aperture, increase the grating-lobe-free steering range, and reduce the beamwidth.)

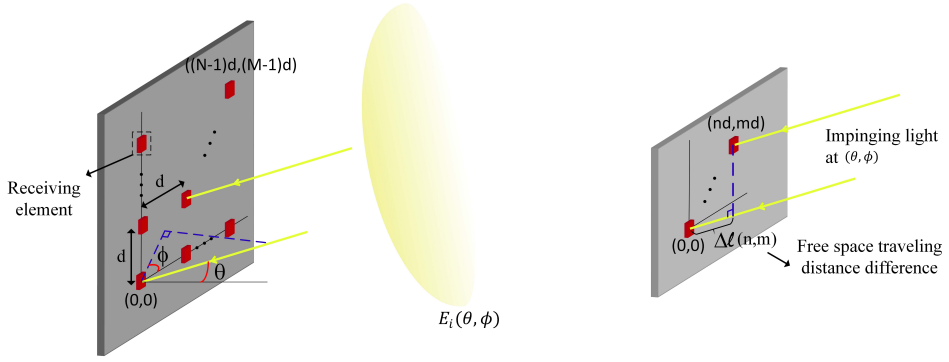

(a) (b)

Fig. 1. (a) The general setting of the receiver operation (b) Free space traveling distance difference between elements for a plane wave impinging at an angle (θ, ϕ).

Assuming $E_i(\theta, \phi)$ is the complex amplitude of the electric field impinging at an angle (θ, ϕ), the electric field coupled to the guided mode of the waveguide by the element at $(0, 0)$ is

$$E(0,0) = \int_0^{2\pi} \int_0^{\pi} G(\theta, \phi) E_i(\theta, \phi) d\theta d\phi, \tag{2}$$

Here, $G(\theta, \phi)$ is the element reception pattern of a single receiving element that quantifies the strength of the electric field coupling for a plane wave with a Poynting vector in the direction of (θ, ϕ) assuming a matched polarization (In the case of a different polarization, the rest of the analysis still holds with the addition of a polarization matching factor). For other elements, the incident plane wave at the angle (θ, ϕ) has a different free-space traveling distance compared to the element at $(0, 0)$ (Fig. 1(b)). This path difference for an element at (nd, md) is

$$\Delta l(n, m) = nd \sin\theta \cos\phi + md \sin\theta \sin\phi, \tag{3}$$

which corresponds to a phase shift of $(2\pi/\lambda)\,\Delta l(n, m)$ for a coherent light of wavelength λ. Therefore, the electric field coupled into the waveguide associated with this receiving element is

$$E(n, m) = \int_0^{2\pi} \int_0^{\pi} G(\theta, \phi) E_i(\theta, \phi) \exp^{-i\frac{2\pi}{\lambda}\Delta l(n,m)} d\theta d\phi. \tag{4}$$

The set of coupled (received) electric field values, $\{E(n, m)\}$, by all the elements can be used to reconstruct the incident wavefront, $E_i(\theta, \phi)$, at every angle (θ, ϕ). The number of receiving elements and their location have a direct impact on the accuracy of this reconstruction. For an exact reconstruction of $E_i(\theta, \phi)$, the whole incident plane should be sampled, which corresponds to an infinite number of elements in both x and y directions. However, the number of receiving

Optics EXPRESS

elements and consequently the aperture size is finite in practical implementations. The effect of the limited aperture size is analogous to the diffraction limit in conventional optical systems.

One powerful approach for reconstructing $E_i(\theta, \phi)$ is forming a linear combination of the samples $E(n, m)$ with complex coefficients, $b_{(n,m)}(\theta_0, \phi_0)$ for the angle (θ_0, ϕ_0). This approach is physically equivalent to applying a set of phase shifts of $\angle b_{(n,m)}(\theta_0, \phi_0)$ and a set of amplitude gains of $|b_{(n,m)}(\theta_0, \phi_0)|$ to the corresponding wavefront. This is similar to the function of a lens which applies different phase shifts to different parts of the wave-front. However, the geometry of the lens is determined upon fabrication and it does a specific manipulation to the wave-front. Using the approach presented, any phase and amplitude control can be adaptively applied to the captured waveform on the chip. In this demonstration, we used a tunable phase shifter for each captured sample. Therefore, any conventional lens function can be realized adaptively on the chip. Because the phases are adjusted precisely on the chip, the equivalent of surface irregularity of conventional lenses is much lower. Essentially, the equivalent lens is $1.55\mu m$ thick and has less than 2nm surface roughness control.

In phased array processing [38], the phase shift of

$$\Delta\phi(n, m) = \frac{2\pi}{\lambda}(nd \sin\theta_0 \cos\phi_0 + md \sin\theta_0 \sin\phi_0), \tag{5}$$

is applied to the received signal captured by the element at (n, m), $E(n, m)$. This phase shift compensates for the phase difference of the captured samples from angle (θ_0, ϕ_0). Therefore, by applying this phase shift, received signals from all the elements will be in phase for the light incident at (θ_0, ϕ_0). The result of the summation is

$$\begin{aligned} E_R(\theta_0, \phi_0) &= \sum_{n=0}^{N-1}\sum_{m=0}^{M-1} E(n, m)e^{i\Delta\phi(n,m)} \\ &= \sum_{n=0}^{N-1}\sum_{m=0}^{M-1}\int_0^{2\pi}\int_0^{\pi} G(\theta, \phi)E_i(\theta, \phi)\exp^{i(\Delta\phi(n,m)-\frac{2\pi}{\lambda}\Delta l(n,m))}\, d\theta d\phi. \end{aligned} \tag{6}$$

$$E_R(\theta_0, \phi_0) = \int_0^{2\pi}\int_0^{\pi} G(\theta, \phi)P(\theta, \phi, \theta_0, \phi_0)E_i(\theta, \phi)d\theta d\phi. \tag{7}$$

$$P(\theta, \phi, \theta_0, \phi_0) = \sum_{n=0}^{N-1}\sum_{m=0}^{M-1} e^{-i\frac{2\pi d}{\lambda}\left[n(\sin\theta\cos\phi-\sin\theta_0\cos\phi_0)+m(\sin\theta\sin\phi-\sin\theta_0\sin\phi_0)\right]}. \tag{8}$$

$P(\theta, \phi, \theta_0, \phi_0)$ is the pattern of the array for the angle (θ_0, ϕ_0) and depends on the element spacing, d, as well as the number of elements in each direction, N and M, for a given wavelength. The product of the array pattern and the receiving element pattern, $G(\theta, \phi)\ P(\theta, \phi, \theta_0, \phi_0)$, is the total pattern of the processing chain and determines the reception gain of the receiver from each direction. Such a function in Fourier optics is usually called the point spread function, PSF. The total pattern has the shape of a beam with a larger value for $(\theta = \theta_0, \phi = \phi_0)$ compared to the other angles. Therefore, light impinging at the angle (θ_0, ϕ_0), $E_i(\theta_0, \phi_0)$, survives the integral of eq. (7) while light at other angles are suppressed. In the OPA receiver, by applying associated phase shifts for different angles, $P(\theta, \phi, \theta_0, \phi_0)$ is formed for each angle and collects $E_R(\theta_0, \phi_0)$.

The proof-of-concept OPA receiver presented in this paper uses an 8-by-8 array of compact and efficient nano-photonic antennas used as receiving elements to form the receiving aperture. Each antenna captures the incident light and couples it into a waveguide. The design of the receiving antenna is shown in Figs. 2(a) and 2(b). The nano-photonic antenna operates similarly to a standard grating coupler [39], but it is optimized to couple the electromagnetic wave at $\lambda = 1,550nm$ to an on-chip dielectric waveguide in a more compact footprint of $5\mu m$ by $2\mu m$. It

Optics EXPRESS

consists of three silicon slabs and a tapered quadratic mode converter that couples the collected light into the waveguide mode. Two etch levels are used in the design of the antenna and the spacing between the slabs is optimized to achieve the maximum coupling efficiency. The reception pattern and the effective aperture of the antenna is shown in Figs. 2(c) and 2(d), respectively. It has a maximum effective collecting area of $1.33\mu m^2$ at $-8.6°$. Moreover, the effective aperture of the antenna varies with the wavelength of the incident light that determines the optical bandwidth of the system (here, the 3dB bandwidth of the antenna is 43nm).

The nano-photonic antennas are placed in an 8-by-8 uniform array with an element spacing $d = 11.2\mu m$ that determines the 8° grating-lob-free FOV. The spacing between the elements in a single photonic layer implementation is limited by the size of the antenna, size of the waveguides used for routing the received signals, and the minimum spacing between the waveguides to avoid coupling. The same limitations appear in OPA transmitters, for which some novel techniques such as sparse [18] and non-uniform [17] element placement and multi-layer photonics [40, 41] have recently been proposed to reduce the element spacing and increase the steering range. These techniques are also applicable to the receiver design to reduce the element spacing and increase the FOV. Figure 2(c) shows the placement and routing of the elements in the 8-by-8 array.

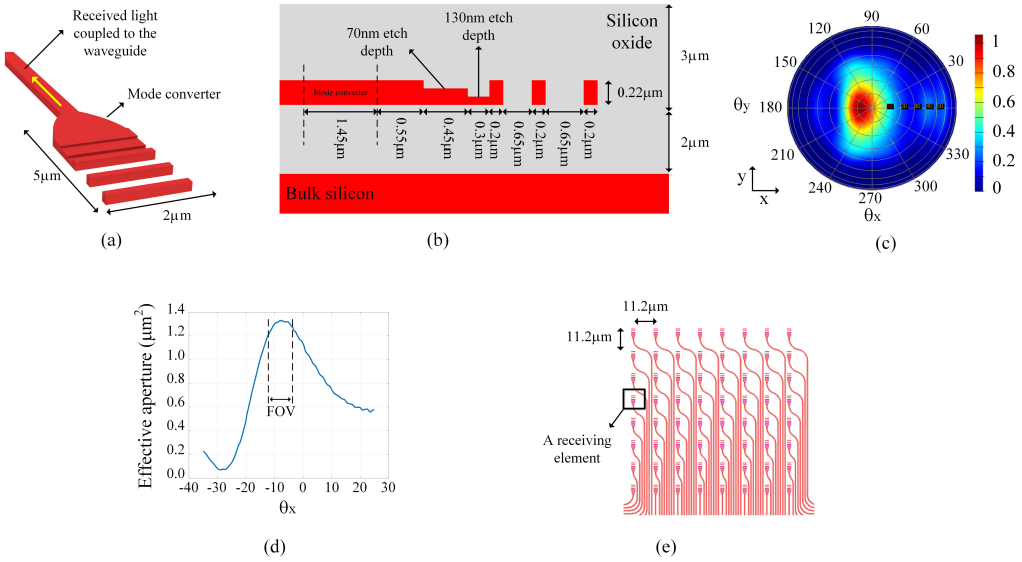

Fig. 2. (a) A single receiving element (b) cross section of the receiving element with detailed dimensions (c) Reception pattern of a single element, $G(\theta, \phi)$ (d) Effective aperture of the receiving element versus θ_x (e) The 8-by-8 array of receiving elements.

Figure 3 shows the array pattern ($P(\theta, \phi, \theta_0, \phi_0)$) for the array structure designed in this paper at ($\theta_0 = 0, \phi_0 = 0$) for two different element spacings. The beam toward ($\theta_0 = 0, \phi_0 = 0$) is called the main lobe. This beam has a finite width due to the finite size of the aperture similar to the diffraction limit for imaging systems and lenses.

$P(\theta, \phi, \theta_0, \phi_0)$ also depends on λ/d. If $d \leq \lambda/2$, then only the main lobe is present and $E_i(\theta, \phi)$ can be reconstructed for $0 \leq \theta \leq \pi/2$ and $0 \leq \phi < 2\pi$. For $d > \lambda/2$, other lobes, called grating lobes [42] in phased array vernacular, also appear in the pattern because of the periodicity of $e^{i\theta}$ with period 2π (eq. (8)). Grating lobes can pick up unwanted signals from directions other than the main lobe direction and thus aliasing occurs as predicted by sampling theory. These grating lobes can be suppressed by the element pattern, $G(\theta, \phi)$, or by a physical spatial filter. Therefore, aliasing defines the field of view of the system which means the maximum range of the angles

Optics EXPRESS

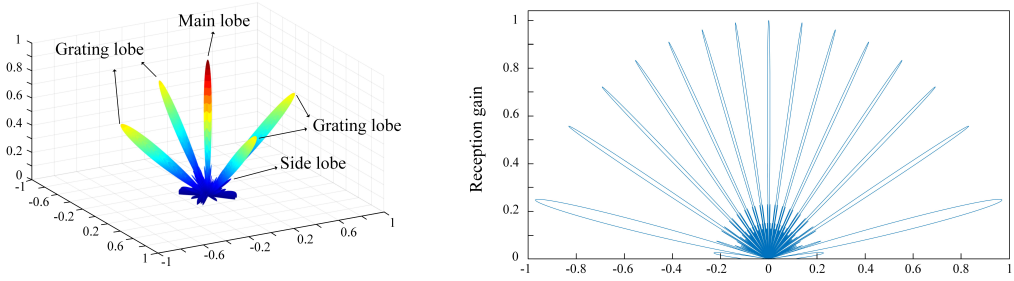

(a) (b)

Fig. 3. (a) Array pattern of an 8-by-8 array with $d/\lambda = 1.3$ and $(\theta_0 = 0, \phi_0 = 0)$ (b) Array pattern of the designed OPA receiver for $\phi = 0$ and $(\theta_0 = 0, \phi_0 = 0)$ (element spacing = $11.2\mu m$). It is assumed that one side of the chip is blocked and light impinging on the aperture comes only from $0 \leq \theta \leq \pi/2$

(θ, ϕ) that can be captured by the system and reconstructed which is the grating-lobe-free steering range. There are also some minor picks in $P(\theta, \phi, \theta_0, \phi_0)$ that are called side lobe [42]. Side lobes decrease as the number of elements in the array increases.

2.2. Optoelectronic mixer

The captured light by the receiving elements can be a weak signal. A good performing receiver should amplify the signal for detection while introducing a minimum extra noise. The minimum signal strength that the receiver can detect defines the sensitivity of the system. In electronic receivers, to reduce the effect of the noise added by the receiver blocks, a low-noise amplifier is usually used at the first stage of the receiver. Therefore, the signal is amplified, and the detrimental effect of the noise of the subsequent stages is suppressed. Such a low noise amplifier is not available for the optical domain. The optical signal can be converted to an electrical signal using a photodetector, and an electronic low-noise amplifier can be used to increase the signal level and make it robust to the noise. However, the loss and noises up to the first electronic amplifier including the photodetector noises affect the signal-to-noise ratio severely.

In this paper, to overcome the optical loss and noises introduced through the processing chain, an optoelectronic down-conversion mixer is designed. The mixer combines an optical reference light with a signal captured by a receiving element. It amplifies the received signal and down-converts its frequency into a radio frequency that can be processed by electronic circuitries while preserving the signal information. Therefore, manipulation of the received optical wavefront can be performed in the electronic domain with stronger signal processing tools.

Figure 4 shows the block diagram of the designed optoelectronic mixer. It includes a PiN diode phase shifter in the reference path, a directional coupler, and two photodiodes for balanced detection. All of these components are integrated on the chip. An epitaxially grown germanium layer is used to form the photodiodes. The germanium layer used in each photodiode is $16\mu m \times 4\mu m$ in size. The mixer has two optical input ports and one electrical output port. The input ports are fed with the received and the reference signals and the current at the output port is the result of the down-conversion. The PiN phase shifter in the reference path to control the output phase. The phase shifters are realized using pin-diodes which operate based on the carrier injection effect [43]. Each phase shifter can provide more than 2π phase shift which is controlled by adjusting the current passing through the PiN diode. The cross section of the fabricated PiN diode phase shifter is shown in Fig. 5(a). A p+ and an n+ region form the anode and cathode

Optics EXPRESS

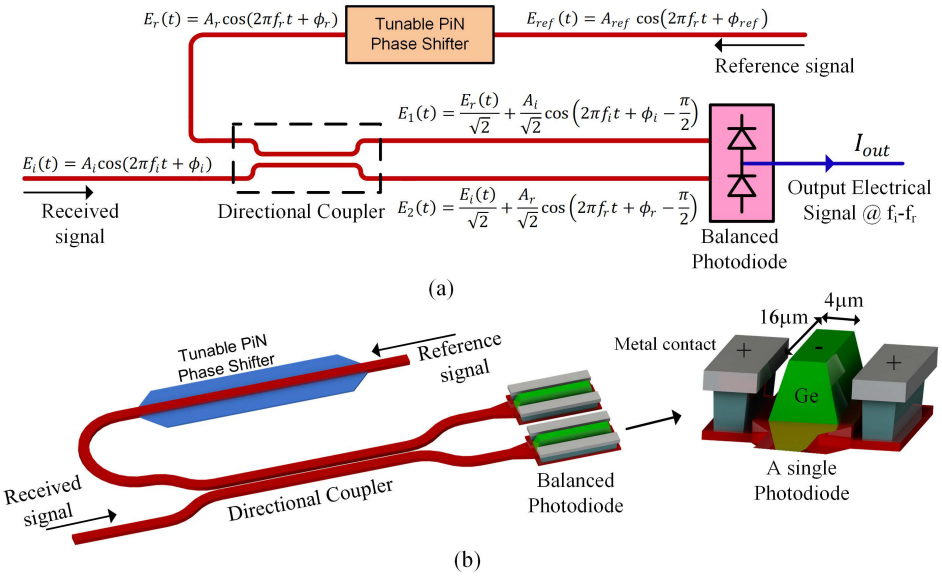

Fig. 4. (a) Block diagram of the optoelectronic mixer (b) simplified drawing of the integrated optoelectronic mixer.

of the diode, respectively. In addition, the silicon waveguide is the intrinsic region of the PiN diode. The doped regions are far enough from the optical path (Fig. 5) to avoid the optical mode interfering with them and causing optical loss. This structure is $500\mu m$ long and provides a 2π phase shift with $28mA$ of injected current. There is a $25\mu m$ spacing between the optoelectronic mixers that results in negligible thermal and electrical cross-talk.

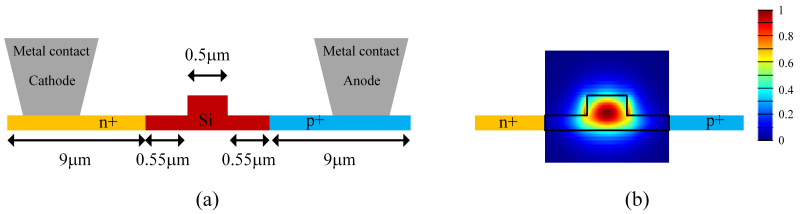

Fig. 5. (a) Structure of the PiN diode phase shifter (b) Optical mode propagating inside the phase shifter (the doped regions do not interfere with the optical mode, avoiding optical insertion loss).

The mixer also includes a 90-degree hybrid directional coupler [44, 45] and a balanced photodiode [46]. The received light and the phase shifted reference signal, which are

$$E_i(t) = A_i \cos(2\pi f_i t + \phi_i), \tag{9}$$

$$E_r(t) = A_r \cos(2\pi f_r t + \phi_r), \tag{10}$$

respectively, are fed into the two input ports of the directional coupler. As a result, each output arm of the directional coupler yields the sum of the two input signals with half of the total input power. Moreover, there is a 90° phase shift inherent to the functionality of the directional coupler

Optics EXPRESS

when a signal is transfered to the through port [45]. Therefore, the envelope or beat component of the two output ports are 180° out of phase.

$$E_1(t) = \frac{1}{\sqrt{2}}\left(A_r^2 + A_i^2 + 2A_rA_i\cos(2\pi(f_i - f_r)t + \phi_i - \phi_r - \pi/2)\right)^{\frac{1}{2}} \cos\left(2\pi\frac{f_i + f_r}{2}t + \psi(t)\right). \quad (11)$$

$$E_2(t) = \frac{1}{\sqrt{2}}\left(A_r^2 + A_i^2 + 2A_rA_i\cos(2\pi(f_i - f_r)t + \phi_i - \phi_r + \pi/2)\right)^{\frac{1}{2}} \cos\left(2\pi\frac{f_i + f_r}{2}t + \psi(t)\right). \quad (12)$$

equations (11) and (12) show the outputs of the directional coupler in the form of the envelope and the optical carrier at frequency $(f_i + f_r)/2$. These signals are fed into the photodiodes, producing currents proportional to the optical power (the envelope of the optical signal squared, divided by two [46,47]). Thus, the output current is

$$\begin{aligned} I_{out}(t) &= (RA_r)A_i \sin(2\pi(f_i - f_r)t + \phi_i - \phi_r), \\ &= 2R\sqrt{P_rP_i}\ \sin(2\pi(f_i - f_r)t + \phi_i - \phi_r), \end{aligned} \quad (13)$$

in which R is the responsivity of the photodiode and $(f_i - f_r)$, beat component frequency, is a few Megahertz. Megahertz is chosen here because it is more convenient for electronic processing. In general, any frequency at which electronic components can operate could be chosen based on the requirements of the design. Equation (13) shows that the amplitude of the received signal is preserved in the output current and the amplitude of the reference signal appears as a gain factor. In a 50Ω system, the gain factor corresponds to the power gain of $P_{electrical}/P_i = 100R^2P_r$ (compared to the direct detection where $P_{electrical}/P_i = 100R^2P_i$, heterodyne detection provides an added conversion gain of P_r/P_i). This feature can be used to amplify the signal power in the optical domain at the first stage of the receiver chain. In addition, the phase of the output current includes the phase of the received signal, ϕ_i, and the reference signal, ϕ_r, which can be adjusted through the tunable phase shifter. For phased array processing, the phase ϕ_r can be adjusted to be $\Delta\phi(n,m)$ for the receiving element at (n,m).

One of the advantages of this design is that the phase shifter is not in the received signal path and does not disturb it, which results in higher sensitivity of the system and ability to detect weaker received signals. Moreover, amplitude control can be realized through controlling the reference signal amplitude or by amplification of $I_{out}(t)$ in the electrical domain. Another advantage of this design is that the stray light and interferers that reach the photodiode can be easily filtered electronically since they do not have effectively any frequency component at $(f_i - f_r)$. Moreover, since the frequency of the output signal is far from DC, $1/f$ noise components of the post-processing electronic blocks can also be filtered.

As explained above, both gain and phase of the output mixed component can be controlled via controlling the phase and amplitude of the reference signal. Phase shifting in the optical domain is especially desired since a simpler and more accurate phase shifter can be implemented in the optical domain. On the other hand, amplitude control can be done in the electrical domain more efficiently. Since both the phase and amplitude information are maintained in the down-converted signal, any processing of interest can be performed in the electrical domain.

With the conversion gain of the optoelectronic mixer, RA_r, the receiver system operates in the shot noise limited regime and all other noises in the receiver chain become negligible. By increasing the reference signal level, the mixed component gets larger while the shot noise of the photodiode due to the dark current and the noises of the electronic circuits that process the photodiode output current stay the same. The total current of a single photodiode is

$$I_{tot} = \frac{I_{out}}{2} + I_{Dark} + \frac{RP_{ref}}{2N_{rx}} + \frac{RP_{Rx}}{2}. \quad (14)$$

in which P_{ref} is the total reference power, P_{Rx} is the received signal powers, I_{Dark} is the dark current flowing through the photodiode, and the number of receiver element in the phased array is denoted by N_{rx}. For a particular reception angle, the signals from the balanced detectors add coherently. Therefore, the total signal to noise ratio, SNR, of the receiver phased array is

$$SNR = \frac{P_{signal}}{P_{noise}} = \frac{N_{rx}(2R^2 P_{ref} P_{Rx}/N_{rx})}{(4eI_{tot} + \overline{I^2}_{n,TIA})BW} \cong \frac{N_{rx} R P_{Rx}}{BW(e + \frac{2N_{rx} I_{Dark} + \overline{I^2}_{n,TIA}}{2RP_{ref}/N_{rx}})}, \tag{15}$$

with $\overline{I^2}_{n,TIA}$ the current noise power spectral density of the electronic circuitry referred to the input of the transimpedance amplifier (TIA), BW the signal bandwidth, and e the charge of an electron. By increasing P_{ref}, the system SNR is limited by the shot-noise of the photodiodes,

$$SNR \cong \frac{N_{rx} R P_{Rx}}{eBW}. \tag{16}$$

At this limit, SNR depends only on the total received signal power collected by all the receiver elements and can be improved by having a larger number of receiving elements. As a result, this system is robust to the detrimental noise sources in the detection chain.

2.3. Design and fabrication of the OPA receiver

The OPA receiver system demonstrated in this paper is fabricated on an SOI substrate. A silicon layer of 220nm hight with two etch levels of 70nm and 130nm is used for designing optical components. The 8-by-8 array elements, Fig. 2, collect the incident light on the OPA aperture. On-chip, low-loss, single-mode dielectric waveguides $0.5\mu m$ in width are used for routing the optical signals. Every sampled signal is routed to an optoelectronic mixer and mixed with the reference signal. The output signal of the optoelectronic mixers contains the amplitude and phase information of the received optical signals but at a MHz carrier frequency which can be processed easily by a simple electronic circuitry.

Figure 6(a) shows the simplified architecture of the designed OPA receiver with 4 elements. To perform phased array processing, the output nodes of the mixers are connected which realizes the summation in eq. (6) since the output currents add based on the Kirchhoff current law. The phase shifters of the optoelectronic mixers can be adjusted to be $\Delta\phi(n, m)$ for the receiving element at (n, m). Therefore, the total output current is the phased array output signal which is routed off-chip for electronic amplification and processing.

The reference light is coupled to the chip through a grating coupler. It is then input to a 6-level binary splitter tree which results in 64 equal-power branches. Each branch is routed to one of the optoelectronic mixers. The pin-diode phase shifters can be controlled independently through their electrical nodes. The cathode nodes of all the pin-diodes are connected to the electrical ground. The anodes are routed to an electrical pad to be accessed via off-chip circuitry. Figure 6(b) shows the fabricated chip and the zoomed in images of the building blocks.

3. Characterization and measurement

To characterize the phase shift provided by the PiN diode phase shifter, a Mach-Zehnder interferometer (MZI) structure is formed with the phase shifter in one of the arms, as shown in Fig. 7(a). The input light is split into two branches and combined at the output. The output optical power varies as a function of the phase shift provided by the phase shifter, with a maximum value for zero phase shift and minimum (ideally zero) for π phase shift. Figure 7(b) shows the MZI output power and the the calculated phase shift versus the injected current. The phase shifter provides a π phase shift with 14mA of injected current. The loss and the power consumption of the phase shifter versus the injected current is also characterized (Fig. 7(c)), showing a

Optics EXPRESS

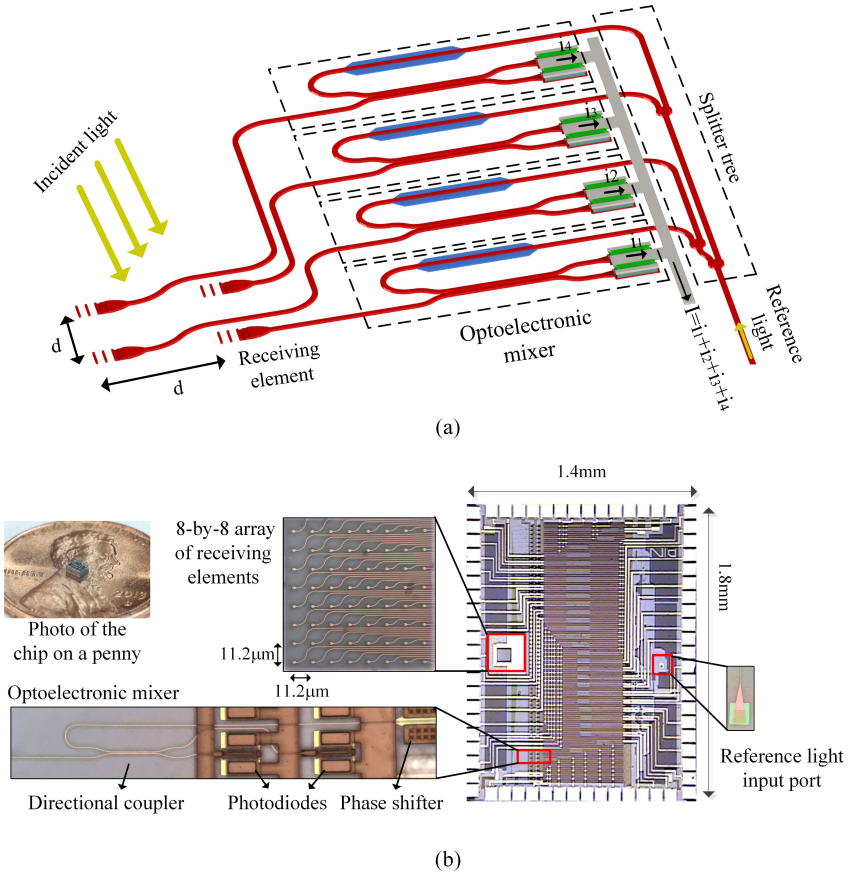

Fig. 6. (a) A simplified diagram of the receiver architecture with a 2-by-2 array aperture. (b) Photo of the fabricated chip and the building blocks.

small insertion loss of 0.3dB and an active loss of 0.17dB/mA. Since the phase shifter is in the reference path, it does not disturb the weak received signal. Different reference levels for different mixers result in an amplitude distribution for the output currents of the mixers. This amplitude distribution has no effect on the beam forming capability, but increase the side lobe levels (amplitude control in the optical or electrical domain can be used to adjust the amplitude of the individual received signals). PiN diode phase shifters can be designed to operate in the GHz range using integrated electronics and traveling wave structures [43]. The measured bandwidth of the PiN diodes used in this work is 707MHz which is limited by the wire-bonds and the bonding pads.

The responsivity of an individual photodiode is measured to be 0.4A/W. There are 128 photodiodes in all the optoelectronic mixers whose output nodes are connected to the output of the system. Since their current noises are independent, the total output current noise power is the sum of the individual diode's noise power. Figure 8 shows the dark current of a single photodiode versus the applied reverse bias. Here, we used 0.5V reverse bias for the photodiode to have enough dynamic range as well as low dark current associated noise. The total dark current of the photodiodes is $2\mu A$, which corresponds to the current noise power of $6.4 \times 10^{-25} A^2/Hz$.

The measurement setup is shown in Fig. 9, in which the OPA receiver chip is mounted on a

Optics EXPRESS

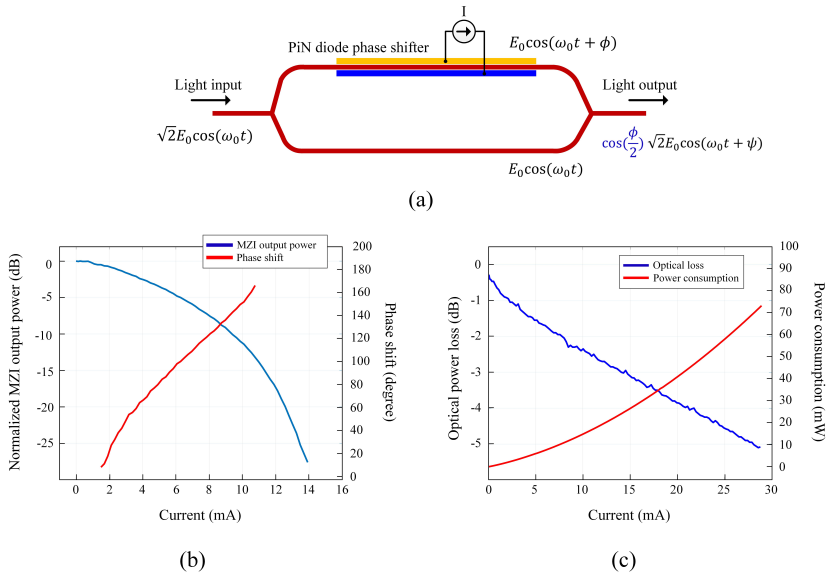

Fig. 7. (a) PiN diode phase shifter is placed in an MZI structure for characterizing the phase shift versus injected current (b) Output power of the MZI versus the electrical current passing through the diode, and the calculated associated phase shift of the PiN diode (c) Loss and power consumption of the PiN diode phase shifter versus electrical current passing through the diode.

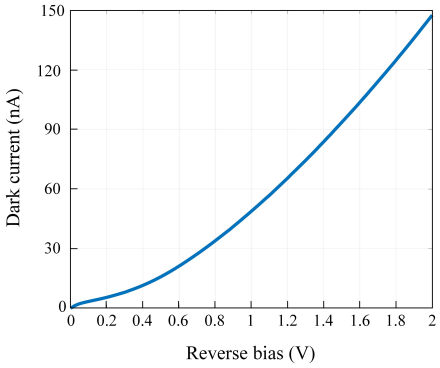

Fig. 8. Dark current of a single photodiode versus the applied reverse bias.

Optics EXPRESS

printed circuit board (PCB) for characterization. The PCB includes sixty-four driver blocks to power the phase shifters embedded in the optoelectronic mixers. Each driver consists of a 10-bit digital to analog converter (DAC), followed by an amplifier and a resistor. Each DAC is input a 10-bit binary value which results in a proportional analog voltage at the output of the amplifier. By controlling the output voltage of the amplifier, the current flowing through the phase shifter and consequently its associated phase shift is adjusted. The resistor at the output of the amplifier is in series with the on-chip pin-diode phase shifter and results in a wider dynamic range and more linearity to control the current flowing through the phase shifter. DACs are controlled with a micro-controller which is the interface between a desktop computer and the PCB. The desired values for the sixty-four DACs are generated by the computer and transferred to the DACs via the micro-controller which results in the corresponding phase shifts.

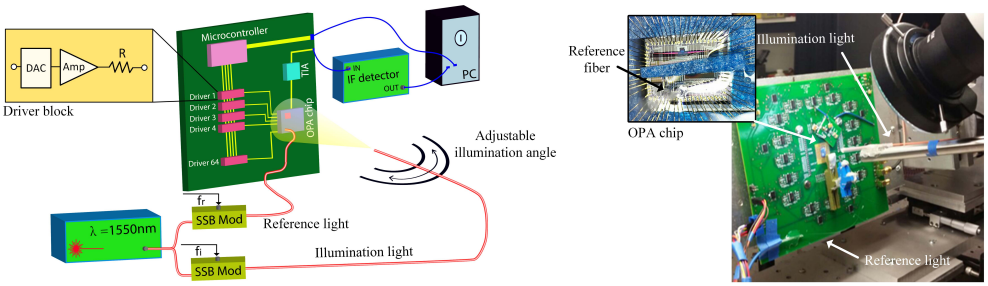

Fig. 9. (a) Diagram of the measurement setup (b) Measurement setup.

The output signal of the chip, which is the sum of the photodiode currents is amplified with a low noise TIA. The TIA also provides a proper bias voltage for the photodiodes. The output voltage of the amplifier is captured by an intermediate frequency (IF) detector that sends the measured amplitude of the mixed component to the computer. Thus, a fully controlled interface is formed such that the computer can change the phase shifts by setting the DAC values and measure the output received signal. DAC values are transfered to the micro-controller through a serial link that determines the speed of the interface. However, this is not a fundamental limitation and a customized integrated circuit chip can be designed to reduce the adjustment time. Moreover, varying power consumption of the phase shifters for different phase shift results in substrate temperature variation with about 20ms of settling time. For fast beamforming and steering, dummy heaters and on-chip temperature sensors can be used [18].

As eq. (13) suggests, if the phases of the illumination and the reference light vary over time due to the phase noise of the laser, the difference of the phase noises appears as a phase noise component at the output mixed signal $(\phi_i(t) - \phi_r(t))$. In the case of using two different lasers for reference and illumination light, the phase noise components of the two lasers (which are independent) add up degrading the sensitivity of the system [48]. Thus, using two lasers necessitates a locking mechanism between the two lasers if a high sensitivity is desired. On the other hand, if the same source is used to generate the two lights, the phase noise components will differ by a time delay $(\phi_i(t) = \phi_r(t - \tau))$. Thus, by minimizing the time delay between the two paths, the subtraction will have a small residue, and the phase noise term at the output current will be diminished. Therefore, in this setup, a single laser source of 1,550nm in wavelength with 100kHz of line-width is used to generate both reference and illumination signals. The laser light is split into two paths, and two single-sideband (SSB) modulators are used to shift the optical frequency of the illumination and reference light by $1.15MHz$ and $-1.75MHz$ respectively. As a result, the output current frequency is $f_i - f_r = 2.9MHz$. While having an SSB modulator on

Optics EXPRESS

only one of the paths suffices, having them on both paths improves the extinction ratio of the mixed component over residual harmonics due to SSB modulators non-idealities.

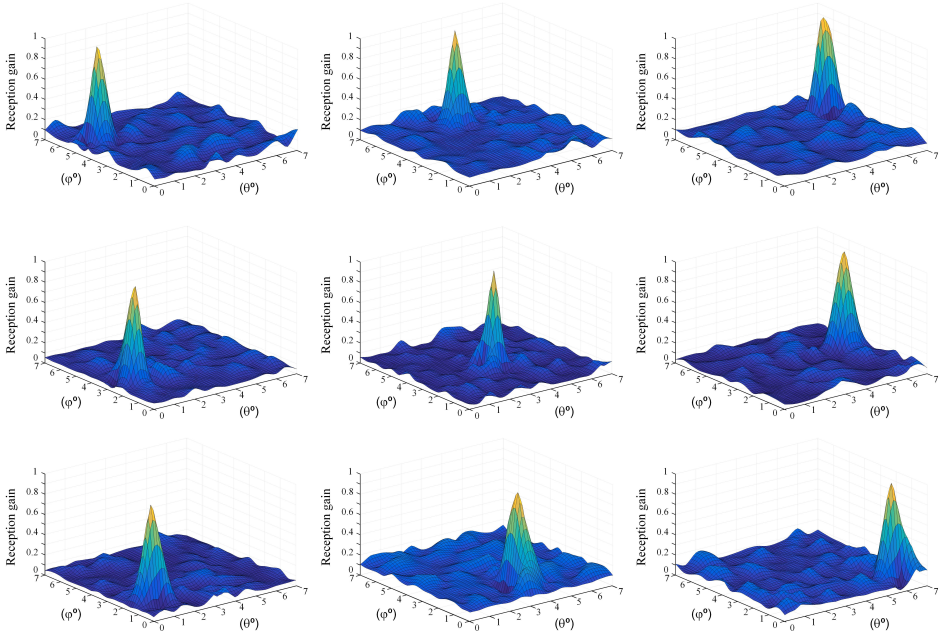

Fig. 10. Measured reception pattern for various angles.

The fiber carrying the reference light is fixed on the chip with a transparent glue such that the light couples into the on-chip reference path through the reference grating coupler with a coupling loss of 6dB. The reference signal is then split into 64 branches and routed to the optoelectronic mixers via on-chip dielectric waveguides. The waveguides have a negligible loss of 2dB/cm, and each splitter has a 0.3dB insertion loss. The illumination fiber is used to illuminate the chip from different angles for beamforming and pattern measurement. By adjusting the phase shift provided by each phase shifter (based on eq. (5)), a reception beam at different angles is formed. To measure the reception pattern, $P(\theta, \phi, 0, 0)$, the illumination fiber is rotated to different angles of (θ, ϕ) and the amplitude of the output current is recorded. The measured beamwidth and side lobe suppression for $P(\theta, \phi, 0, 0)$ are 0.75° and 10dB respectively. To form a beam at a different angle (θ_0, ϕ_0), a set of phase shifts corresponding to that angle should be programmed through the DACs. Therefore, each angle has an associated DAC setting which can be applied to form a beam in that direction. Figure 10 shows the measured pattern for several angles (θ_0, ϕ_0). We observed no phase shifter drift and the measured patterns are repeatable when measured over different time spans.

To characterize the sensitivity of the receiver, eq. (15) is used to determine the required reference power. The TIA is a two-stage amplifier with a transimpedance gain of $120,000\Omega$, which is sufficient to avoid signal degradation due to the IF detector internal noise. Based on this transimpedance gain, a 1pA photo-current results in a 120nV of output voltage, and thus -125dBm output power in a 50Ω system. The measured output noise by the IF detector in the absence of the optical signals (total electronic circuitry and photodiodes dark current associated noise) is -97dBm/Hz. This translates to $6.9 \times 10^{-22} A^2/Hz$ when it is referred to the input of the TIA. Equation (15) suggests that to achieve the maximum sensitivity, the shot noise due to the reference signal should dominate other noise sources which means

Optics EXPRESS

$2eRP_{ref} >> 6.9\times10^{-22}A^2/Hz \quad (P_{ref} >> 5.5mW)$. In practice, we achieved 3dB higher noise floor (Fig. 11) with $P_{ref} = 15dBm$. Considering the 6dB fiber to chip coupling loss and 1.8dB total splitter-tree loss, this value is in agreement with the theory. In this setting, reference power delivered to each optoelectronic mixer is $-11dBm$, which corresponds to a mixer gain of $79dB$ for a -90dBm (1nW) received signal. For this level of reference power, the effects of the TIA and photodiode noise is neglected, resulting in the maximum sensitivity of the system.

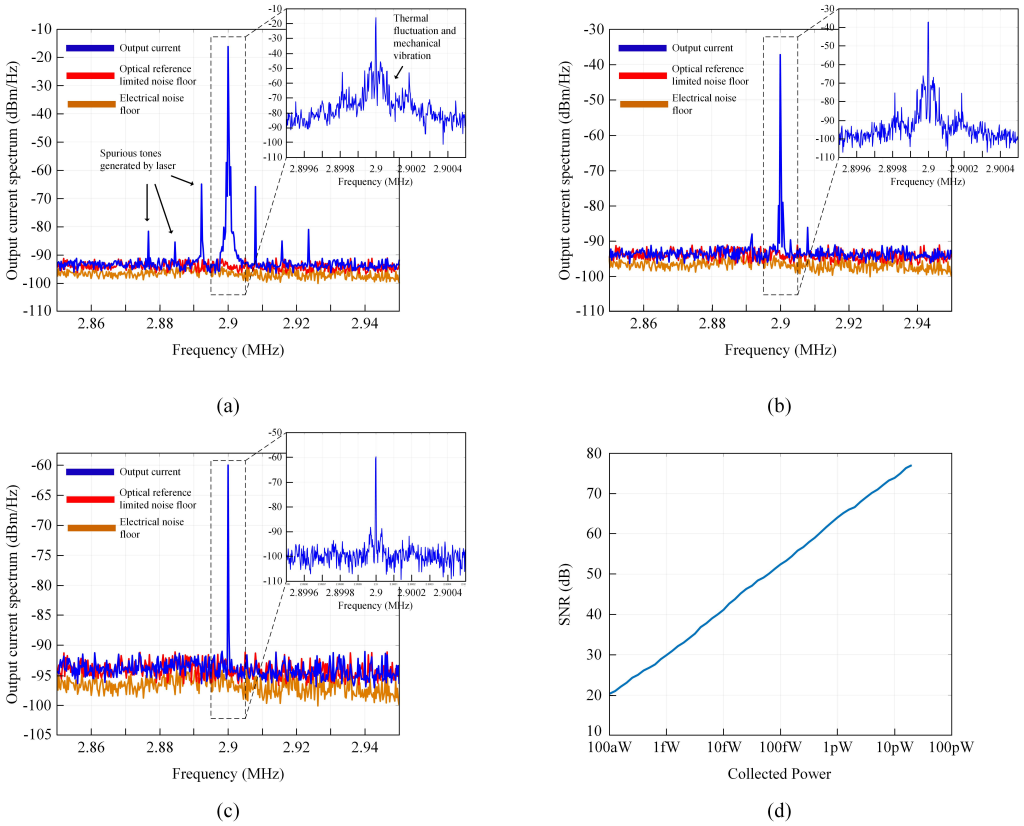

Fig. 11. (a)-(c) Spectrum of the output signal with a 1Hz resolution bandwidth for 20pW, 200fW, and 2fW of collected power respectively. Red curve shows the noise floor due to the shot noise of the reference signal which is adjusted to be well above the electronic noise floor to gain the maximum sensitivity (d) SNR of the detected signal versus collected incident power.

The SNR of the detected signal is measured versus the collected incident power. A fiber is used to illuminate the chip, forming a spot with 7.7mm diameter. The total collection area of the aperture is $64\times1.33\mu m^2 = 85.12\mu m^2$. Figures 11(a)-11(c) show the measured power spectrum of the detected signal for three different collected power levels: 20pW, 200fW, and 2fW. Moreover, the SNR of the detected signal versus the collected power by the receiving elements is shown in Fig. 11(d). There are weak spurious phase modulation tones associated with the laser source that appear in the spectrum of the output signal (Fig. 11(a)). In case the power level of these spurious signals is a limiting factor for an application, a more stable and narrower line-width laser can be used. Moreover, thermal fluctuations and mechanical vibrations that are different in the illumination and reference signal paths (affecting ϕ_i and ϕ_{ref}, respectively) appear in the spectrum of the output signal and limit the close-in SNR to 30dB (Figs. 11(a)-11(c)). These

Optics EXPRESS

variations have a relatively low frequency bandwidth (less than 1KHz). and are not significant in many applications. Due to the multiple elements that are placed in the reference path, there is a total of 10m fiber in each path. Integrating the SSB modulators on the chip will eliminate this path length difference and consequently the thermal and mechanical fluctuation differences.

The directive reception feature of the OPA receiver enables this system to operate as a lens-less camera. As mentioned previously, an OPA receiver can form a reception beam and collect the light incident at an angle selectively while filtering out the others. Moreover, the reception beam can be steered electronically by applying the proper phase shift to the captured light by each element. To demonstrate the imaging capability of the system, an imaging setup as shown in Fig. 12(a) is arranged. As an imaging subject, a sheet of plexiglass covered by copper is patterned to scatter light. This imaging subject is placed in front of the chip and illuminated from the back side. Therefore, the intensity of the light coming toward the chip from the angles associated with the open spots is stronger than the covered areas. The reception beam of the OPA is steered across the field of view and intensity of the light coming toward the chip at each angle is collected. Tiling the information regarding different angles next to each other yields the image of the scene in front of the chip. Figure 12(b) shows the images taken by the 8-by-8 OPA receiver for several imaging subjects. While the 3dB beamwidth of the OPA is 0.75°, to get a clearer distinction between neighboring pixels, a larger angular resolution is used to avoid the signal pick-up by the tail of the reception beam. Here, a 4×4 pixel array is used to provide a clear indication of the image formation details.

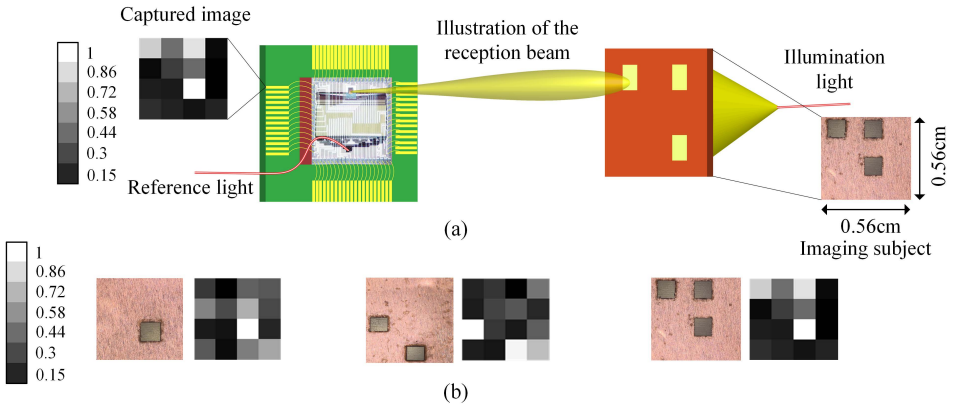

Fig. 12. (a) Setup configuration for lens-less imaging (b) Images taken from imaging subjects.

4. Conclusion

In this paper, an integrated optical receiver architecture is presented that captures samples of the incident light on its aperture and processes it on-chip. The samples are collected by an array of receiving elements. A high-performance optoelectronic mixer is designed to down-convert the optical signals received by each element to a radio frequency in the electronic domain while preserving their phase and amplitude. The mixer provides conversion gain which makes the detection robust to noise sources in the system. Moreover, stray light and interference signals are rejected through heterodyne mixing. Using the adjustable phase shifter of the mixer and gain control in the electronic domain, arbitrary wavefront manipulation can be performed on the set of received signals to achieve the desired operation. The system in effect functions as a thin on-chip adaptive flat optical system. Using this system, the first high sensitivity OPA receiver with a two-dimensional aperture (8-by-8) is presented. The beamforming capability of this receiver chip

Optics EXPRESS

is demonstrated and an object is imaged via electronically steering the reception beam, proving its lens-less imaging capability.

References

1. J. Park, J.-H. Kang, S. J. Kim, X. Liu, and M. L. Brongersma, "Dynamic reflection phase and polarization control in metasurfaces," Nano Lett. **17**, 407–413 (2017). PMID: 27936784.
2. A. Arbabi, Y. Horie, M. Bagheri, and A. Faraon, "Dielectric metasurfaces for complete control of phase and polarization with subwavelength spatial resolution and high transmission," Nat. Nanotechnol. **10**, 937 EP – (2015).
3. M. I. Shalaev, J. Sun, A. Tsukernik, A. Pandey, K. Nikolskiy, and N. M. Litchinitser, "High-efficiency all-dielectric metasurfaces for ultracompact beam manipulation in transmission mode," Nano Lett. **15**, 6261–6266 (2015).
4. N. Mohammadi Estakhri and A. Alù, "Wave-front transformation with gradient metasurfaces," Phys. Rev. X **6**, 041008 (2016).
5. N. Yu and F. Capasso, "Flat optics with designer metasurfaces," Nat. Mater. **13**, 139 EP – (2014). Review Article.
6. Z. Zhu, P. G. Evans, R. F. Haglund, and J. G. Valentine, "Dynamically reconfigurable metadevice employing nanostructured phase-change materials," Nano Lett. **17**, 4881–4885 (2017).
7. J. Sautter, I. Staude, M. Decker, E. Rusak, D. N. Neshev, I. Brener, and Y. S. Kivshar, "Active tuning of all-dielectric metasurfaces," ACS Nano **9**, 4308–4315 (2015).
8. H.-S. Ee and R. Agarwal, "Tunable metasurface and flat optical zoom lens on a stretchable substrate," Nano Lett. **16**, 2818–2823 (2016).
9. Y.-W. Huang, W. T. Chen, W.-Y. Tsai, P. C. Wu, C.-M. Wang, G. Sun, and D. P. Tsai, "Aluminum plasmonic multicolor meta-hologram," Nano Lett. **15**, 3122–3127 (2015).
10. W. T. Chen, P. Török, M. R. Foreman, C. Y. Liao, W.-Y. Tsai, P. R. Wu, and D. P. Tsai, "Integrated plasmonic metasurfaces for spectropolarimetry," Nanotechnology **27**, 224002 (2016).
11. M. Khorasaninejad, W. T. Chen, A. Y. Zhu, J. Oh, R. C. Devlin, D. Rousso, and F. Capasso, "Multispectral chiral imaging with a metalens," Nano Lett. **16**, 4595–4600 (2016).
12. W. T. Chen, K.-Y. Yang, C.-M. Wang, Y.-W. Huang, G. Sun, I.-D. Chiang, C. Y. Liao, W.-L. Hsu, H. T. Lin, S. Sun, L. Zhou, A. Q. Liu, and D. P. Tsai, "High-efficiency broadband meta-hologram with polarization-controlled dual images," Nano Lett. **14**, 225–230 (2014).
13. X. Ni, Z. Jing Wong, M. Mrejen, Y. Wang, and X. Zhang, "An ultrathin invisibility skin cloak for visible light," Science **349**, 1310–1314 (2015).
14. J. Sun, E. Timurdogan, A. Yaacobi, E. S. Hosseini, and M. R. Watts, "Large-scale nanophotonic phased array," Nature **493**, 195 EP – (2013).
15. C. V. Poulton, M. J. Byrd, M. Raval, Z. Su, N. Li, E. Timurdogan, D. Coolbaugh, D. Vermeulen, and M. R. Watts, "Large-scale silicon nitride nanophotonic phased arrays at infrared and visible wavelengths," Opt. Lett. **42**, 21–24 (2017).
16. S. Chung, H. Abediasl, and H. Hashemi, "A monolithically integrated large-scale optical phased array in silicon-on-insulator cmos," IEEE J. Solid-State Circuits **53**, 275–296 (2018).
17. D. N. Hutchison, J. Sun, J. K. Doylend, R. Kumar, J. Heck, W. Kim, C. T. Phare, A. Feshali, and H. Rong, "High-resolution aliasing-free optical beam steering," Optica **3**, 887–890 (2016).
18. R. Fatemi, A. Khachaturian, and A. Hajimiri, "Scalable optical phased array with sparse 2d aperture," in *Conference on Lasers and Electro-Optics,* (Optical Society of America, 2018), p. STu4B.6.
19. F. Aflatouni, B. Abiri, A. Rekhi, and A. Hajimiri, "Nanophotonic projection system," Opt. Express **23**, 21012–21022 (2015).
20. J. Notaros, N. Li, C. V. Poulton, Z. Su, M. J. Byrd, E. S. Magden, and M. R. Watts, "Cmos-compatible optical phased arrays with monolithically-integrated erbium lasers," in *Conference on Lasers and Electro-Optics,* (Optical Society of America, 2018), p. STu4B.2.
21. T. Komljenovic and P. Pintus, "On-chip calibration and control of optical phased arrays," Opt. Express **26**, 3199–3210 (2018).
22. J. L. Pita, I. Aldaya, O. J. S. Santana, L. E. E. de araujo, P. Dainese, and L. H. Gabrielli, "Side-lobe level reduction in bio-inspired optical phased-array antennas," Opt. Express **25**, 30105–30114 (2017).
23. C. T. Phare, M. C. Shin, J. Sharma, S. Ahasan, H. Krishnaswamy, and M. Lipson, "Silicon optical phased array with grating lobe-free beam formation over 180 degree field of view," in *Conference on Lasers and Electro-Optics,* (Optical Society of America, 2018), p. SM3I.2.
24. C. Qin, K. Shang, S. Feng, G. Liu, G. Liu, S. Pathak, and S. J. B. Yoo, "1×256 multi-layer, low-loss, si3n4 waveguide optical phased arrays with 0.050° instantaneous-field-of-view," in *Conference on Lasers and Electro-Optics,* (Optical Society of America, 2017), p. STh1M.2.
25. M. R. Kossey, C. Rizk, and A. C. Foster, "End-fire silicon optical phased array with half-wavelength spacing," APL Photonics **3**, 011301 (2017).
26. C. V. Poulton, D. Vermeulen, E. Hosseini, E. Timurdogan, Z. Su, B. Moss, and M. R. Watts, "Lens-free chip-to-chip free-space laser communication link with a silicon photonics optical phased array," in *Frontiers in Optics 2017,* (Optical Society of America, 2017), p. FW5A.3.

Optics EXPRESS

27. S. J. Spector, B. F. Lane, M. R. Watts, L. D. Benney, J. G. Delva, A. E. Hare, A. F. Kelsey, J. M. Mlynarczyk, E. S. Hosseini, C. V. Poulton, and J. P. Laine, "Broadband imaging and wireless communication with an optical phased array," in *Conference on Lasers and Electro-Optics,* (Optical Society of America, 2018), p. SM3I.7.
28. S. A. Miller, C. T. Phare, Y.-C. Chang, X. Ji, O. A. J. Gordillo, A. Mohanty, S. P. Roberts, M. C. Shin, B. Stern, M. Zadka, and M. Lipson, "512-element actively steered silicon phased array for low-power lidar," in *Conference on Lasers and Electro-Optics,* (Optical Society of America, 2018), p. JTh5C.2.
29. C. V. Poulton, A. Yaacobi, D. B. Cole, M. J. Byrd, M. Raval, D. Vermeulen, and M. R. Watts, "Coherent solid-state lidar with silicon photonic optical phased arrays," Opt. Lett. **42**, 4091–4094 (2017).
30. C. V. Poulton, P. Russo, E. Timurdogan, M. Whitson, M. J. Byrd, E. Hosseini, B. Moss, Z. Su, D. Vermeulen, and M. R. Watts, "High-performance integrated optical phased arrays for chip-scale beam steering and lidar," in *Conference on Lasers and Electro-Optics,* (Optical Society of America, 2018), p. ATu3R.2.
31. J. J. López, S. A. Skirlo, D. Kharas, J. Sloan, J. Herd, P. Juodawlkis, M. Soljačić, and C. Sorace-Agaskar, "Planar-lens enabled beam steering for chip-scale lidar," in *Conference on Lasers and Electro-Optics,* (Optical Society of America, 2018), p. SM3I.1.
32. W. Zhang, "Lidar-based road and road-edge detection," in *2010 IEEE Intelligent Vehicles Symposium,* (2010), pp. 845–848.
33. M. A. Khalighi and M. Uysal, "Survey on free space optical communication: A communication theory perspective," IEEE Commun. Surv. Tutorials **16**, 2231–2258 (2014).
34. J. Zhou, J. Sun, A. Yaacobi, C. V. Poulton, and M. R. Watts, "Design of 3d hologram emitting optical phased arrays," in *Advanced Photonics 2015,* (Optical Society of America, 2015), p. IT4A.7.
35. R. Fatemi, B. Abiri, and A. Hajimiri, "A one-dimensional heterodyne lens-free opa camera," in *Conference on Lasers and Electro-Optics,* (Optical Society of America, 2016), p. STu3G.3.
36. R. Fatemi, B. Abiri, and A. Hajimiri, "An 8×8 heterodyne lens-less opa camera," in *Conference on Lasers and Electro-Optics,* (Optical Society of America, 2017), p. JW2A.9.
37. H. Abediasl and H. Hashemi, "Monolithic optical phased-array transceiver in a standard soi cmos process," Opt. Express **23**, 6509–6519 (2015).
38. J. Kraus and R. Marhefka, *Antennas for All Applications* (McGraw-Hill, 2002).
39. X. Chen, C. Li, C. K. Y. Fung, S. M. G. Lo, and H. K. Tsang, "Apodized waveguide grating couplers for efficient coupling to optical fibers," IEEE Photonics Technol. Lett. **22**, 1156–1158 (2010).
40. Y. Zhang, K. Shang, Y.-C. Ling, and S. J. B. Yoo, "3d integrated silicon photonic unit cell with vertical u-turn for scalable optical phase array," in *Conference on Lasers and Electro-Optics,* (Optical Society of America, 2018), p. SM3I.6.
41. W. D. Sacher, Y. Huang, G. Lo, and J. K. S. Poon, "Multilayer silicon nitride-on-silicon integrated photonic platforms and devices," J. Light. Technol. **33**, 901–910 (2015).
42. R. Hansen, *Phased Array Antennas* (Wiley, 2009).
43. D. Marris-Morini, L. Vivien, J. M. Fédéli, E. Cassan, P. Lyan, and S. Laval, "Low loss and high speed silicon optical modulator based on a lateral carrier depletion structure," Opt. Express **16**, 334–339 (2008).
44. X. Chen, R.-D. Wen, and S.-Y. Tseng, "Analysis of optical directional couplers using shortcuts to adiabaticity," Opt. Express **24**, 18322–18331 (2016).
45. D. Pozar, *Microwave Engineering* (Wiley, 2004).
46. B. L. Kasper, C. A. Burrus, J. R. Talman, and K. L. Hall, "Balanced dual-detector receiver for optical heterodyne communication at gbit/s rates," Electron. Lett. **22**, 413–415 (1986).
47. S. Alexander, *Optical Communication Receiver Design* (SPIE Optical Engineering Press, 1997).
48. A. Vasilyev, "The optoelectronic swept-frequency laser and its applications in ranging three-dimensional imaging and coherent beam combining of chirped-seed amplifiers," Ph.D. thesis, California Institute of Technology (2013).